AIMS Energy, 14(1): 259–274.
DOI: 10.3934/energy.2026011
Received: 11 November 2025
Revised: 26 January 2026
Accepted: 06 February 2026
Published: 27 February 2026

https://www.aimspress.com/journal/energy

Research article

Influence of nitrogen gas flow rate on the physical properties of corncob activated carbon for lithium-ion capacitor electrodes

Asih Kurniasari[1,*], Ariono Verdianto[2], Yoyok Dwi Setyo Pambudi[3] and Chairul Hudaya[4]

[1] Research Center for Electrical Technology, Research Organization for Energy and Manufacture, National Research and Innovation Agency, Kawasan Sains Terpadu B.J. Habibie Serpong, Tangerang Selatan, 15314, Indonesia
[2] Production Division, PT PLN (Persero) PUSHALRIS–UP2W III, Bandung 40272, Indonesia
[3] Research Center for Nuclear Reactor Technology, Research Organization for Nuclear Energy, National Research and Innovation Agency, Kawasan Sains Terpadu B.J. Habibie Serpong, Tangerang Selatan 15314, Indonesia
[4] Department of Electrical Engineering, Faculty of Engineering, Universitas Indonesia, Depok 16424, Indonesia

* **Correspondence:** Email: asih.kurniasari@brin.go.id.

Abstract: To address the disadvantages of both lithium-ion batteries (low power density) and supercapacitors (low energy density), lithium-ion capacitors (LICs) were created as a hybrid energy storage system. In this study, the biomass-derived activated carbon from corncob (CACN) was prepared by adopting physical and chemical activation processes under different nitrogen gas flow rates (N_2). The material was activated with KOH and then pyrolyzed at 700 °C under varying N_2 flow rates from 200 to 400 standard cubic centimeters per minute (sccm). Scanning electron microscopy (SEM) images revealed that the surface morphology appears to have a highly porous structure. The highest specific surface area (SSA) (1936 $m^2 g^{-1}$) was achieved following activation at 300 sccm, confirmed by the Brunauer–Emmett–Teller (BET) results. X-ray diffraction (XRD) and Raman spectroscopy indicated that the crystal structure was amorphous. Through electrochemical tests, the quasi-rectangular cyclic-voltammogram (CV) graph of the LIC coin-cell constructed by CACN (LICN) has similar characteristics to capacitors and batteries. The best coulombic stability was found for LIC with CACN activated at 300 sccm, presenting the highest energy and power density (10.79 Wh kg^{-1} and 526.39 W kg^{-1}) by charge-discharge (CD) tests. This optimization of carbon activation enables us to achieve the optimum physical characteristics and electrochemical performance of activated carbon and LIC, respectively.

Keywords: nitrogen gas flow rate; activated carbon; corncob; lithium-ion capacitor; physical properties; electrochemical performance

1. Introduction

The demand for energy storage systems with high energy and power density is increasing due to the growing need for electric vehicles (EVs), renewable energy integration, household electricity supply, and battery backup systems for safety loads in nuclear energy applications [1,2]. Lithium-ion batteries (LIBs) and supercapacitors (SCs) are among the most important energy storage devices used in several applications; however, they cannot fully meet these demands. LIBs are considered promising energy storage systems due to their high energy density, reaching up to 300 Wh kg^{-1} through faradaic reactions [3–5]. However, LIBs suffer from several drawbacks, such as voltage degradation during long-term use and high cycles, lower power densities not exceeding 1 kW kg^{-1}, and relatively slow charging and discharging processes caused by redox reactions. These processes accelerate material degradation and limit the cycle life to 1000 cycles [2,5,6].

In contrast, electric double-layer capacitors (EDLCs), which function as symmetrical supercapacitors, exhibit high power density, reaching 1–2 kW kg^{-1} with carbon-based electrodes and exceeding 3 kW kg^{-1} with advanced materials. This performance stems from rapid ion adsorption-desorption reactions and up to a million charge/discharge cycles [7,8]. Yet, the EDLC performance is limited in energy density, being restricted to less than 10 Wh kg^{-1}, due to their surface-dependent charge storage mechanism and the limited number of ions available in the electrolyte [8–10]. The increasing demand for simultaneous high energy and power supply, for instance, for HEVs and UPS systems, has driven extensive research into hybrid energy storage technologies.

Lithium-ion capacitors (LICs) are a promising technology that combines faradaic and non-faradaic charge storage mechanisms. LICs integrate the structural and electrochemical advantages of LIBs and EDLCs, where the anode uses a high-energy electrode made of lithium graphite material (as in LIBs), the cathode uses a high-power electrode made of highly porous activated carbon (AC) (as in EDLCs), and the organic electrolyte contains Li salt [11–13]. Porous carbon plays a key role in supercapacitor performance, as its high surface area and interconnected pore structure dictate the efficiency of ion adsorption [14,15]. In standard EDLCs, these pores provide the necessary sites for the formation of the electric double layer; in LICs, they facilitate rapid anion transport to balance lithium-ion intercalation at the anode. By optimizing the pore size distribution, these materials minimize internal resistance and facilitate high-rate capabilities [16,17]. With this combined structure, LICs provide redox and adsorption-desorption ion mechanisms during charging and discharging, thereby increasing the specific capacity and maximum voltage. Devices can achieve significantly increased energy densities without sacrificing the rapid discharge characteristic of carbon-based electrodes [3].

Similar to other energy storage systems, material selection is critical for achieving the best performance of LICs. The LIC concept was first introduced by Amatucci GG et al. in 2001 using $Li_4Ti_5O_{12}$ (LTO) as the anode and AC as the cathode, producing a device with an energy density exceeding 20 Wh kg^{-1}, which is 4–5 times higher than that of EDLCs [18]. In 2017, Ruan D et al. developed LICs using microspherical LTO with different Li insertions as the anode and AC as the cathode (LIC 700-F), achieving an energy density of 2466 W kg^{-1} and a capacitance retention of 92% after 10,000 cycles [19]. The fundamental advantages of LTO, particularly its safety and structural

integrity, were comprehensively reviewed by Zhao B et al., who identified it as a premier anode candidate [20]. Furthermore, Zhao S et al. emphasized that the absence of solid electrolyte interface (SEI) formation and its fast-charging capability are the critical factors for its success in hybrid energy storage systems [21]. Additionally, Chen C et al. leveraged LTO's stable matrix to effectively houses silicon, achieving a high capacity of 1,152 mAh g^{-1} by mitigating the mechanical stress typically associated with silicon anode [22]. Gangaja B et al. demonstrated that LTO's performance can be further optimized into a TiO_2 composite, achieving 150 mAh g^{-1} at high currents with an endurance of 5,000 cycles [23]. As such, LTO remains one of the most promising anode materials due to its thermal stability, zero-strain insertion that minimizes volume changes, and the absence of SEI formation.

The cathode also plays a significant role in LIC performance by providing more active sites for charge accumulation, thereby improving energy density, power density, and thermal stability [24,25]. Using LTO, Agrawal R et al. fabricated LICs with graphene and carbon nanotube (G-CNT) as the cathode, achieving an energy density of 7 Wh kg^{-1} and power density of 325 W kg^{-1} [12]. Gao X et al. used Sri Lankan vein graphite as natural graphite and obtained an energy density of 48 Wh kg^{-1} at 7.4 kW kg^{-1} [26]. Commercial activated carbon has also demonstrated excellent performance; Liu C et al. reported a specific capacitance of 140 F g^{-1} [27]. The consistent combination of LTO anodes and carbon-based cathodes has stimulated extensive research on carbon materials to further improve LIC performance.

For large-scale production, electrode materials must be easily produced while maintaining high electrode performance. Biomass-derived carbon electrodes have gained interest due to their low cost, abundant availability, non-toxicity, and ease of fabrication with high porosity and specific surface area (SSA) through activation processes. Sun F et al. produced activated carbon from pomelo peel with a simple KOH activation process, achieving an energy density of 84.6 Wh kg^{-1} at 24375 W kg^{-1} [11]. Sennu P et al. used activated carbon from *Prosopis juliflora* using a KOH with an activation ratio of 1:2 wt%, achieving an energy density of 216 Wh kg^{-1} [28]. Zhang Y et al. developed supercapacitors using AC derived from longan shells employing dual activation using eggshell powder and KOH, achieving a specific energy of 11.6 Wh kg^{-1} and a power output of 87 kW kg^{-1} [29]. SSA, porosity, and other physical properties of AC biomass affect the cathode performance in LIC. The wider the surface area and the range of pore size distribution, the smaller the crystallite (grain), thereby increasing the number of active sites for charge accumulation. These properties can be adjusted in several activation steps, including the mass ratio of the chemical agent, the pyrolysis time, and the temperature [30].

One parameter that is rarely varied during carbon activation is the N_2 flow rate. The N_2 flow helps reduce oxygen-containing groups on the carbon surface. Azargohar R et al. used N_2 flow rates up to 200 standard cubic centimeters per minute (sccm), Magar SD et al. used 110 sccm, and other researchers do not report the flow rate [31–33]. Carbon activation using KOH involves several changes in chemical bonds [34,35]. While parameters like temperature, KOH ratio, and time are commonly studied, the effect of inert gas flow rate, especially above 200 sccm, remains poorly understood. Higher N_2 flow rates are hypothesized to influence KOH intercalation and pore development, thereby increasing surface area and porosity [36].

According to the Indonesian Statistics Agency, corn production reached 19.61 million tons in 2015 and continues to increase by 3.45–4.6 million tons annually. This growth generates large quantities of corncob waste, creating environmental challenges due to its limited economic value [37]. This study aims to convert corncob waste into useful products, such as activated carbon by investigating the effect of varying N_2 flow rate. Corncobs were first carbonized under argon (Ar) flow and subsequently mixed with KOH as the chemical activator. The sample was then activated at 700 °C under N_2 at 200, 300,

and 400 sccm. The resulting activated carbon was used as the cathode material in LIC devices along with commercial LTO as the anode. The results demonstrate that activated carbon prepared under optimized N_2 flow rates significantly improves LIC performance.

2. Materials and methods

2.1. Preparation of corncob activated carbon

In this study, all parts of dried corncob (chaff/beeswing, woody ring, and pitch) were pounded and ground into fine grains, which were then carbonized in a tube furnace at 200 sccm argon flow at 600 °C with a heating rate of 10 °C/min, held for 0.5 h. The corncob carbon was then sifted with a 200 mesh sieve to obtain homogeneous grains, washed to remove impurities, and dried to ensure no water remained. Chemical activation was carried out by mixing the dried corncob carbon with KOH at a weight ratio of 1:2, acting as the chemical activator. This was followed by a pyrolysis step (physical activation) in a tube furnace under the influence of N_2 at 700 °C with a heating rate of 11 °C/min, held for 1 h at different flow rates: 200, 300, and 400 sccm, which were denoted as CACN200, CACN300, and CACN400, respectively. The samples were then washed with diluted HCl and distilled water to neutralize the carbon pH. Finally, CACNs were dried in an oven for 24 h at 120 °C. The finer CACNs were used as the active material for the LIC cathode. This procedure is illustrated in Figure 1.

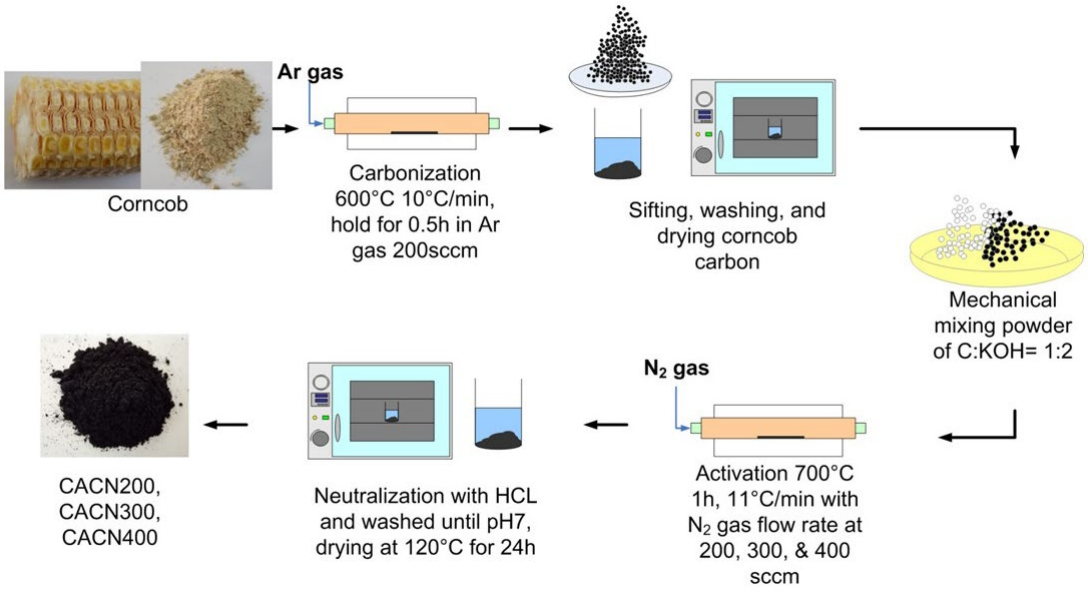

Figure 1. Synthesis process of corncob activated carbon.

2.2. Material characterizations

A scanning electron microscope (SEM) with a ZEISS EVO MA10 500–5000× magnification was used to determine the morphology and microstructure of all samples. Using the same device, one of the samples was then tested to obtain the elemental surface with energy-dispersive X-ray (EDX). The surface area and pore distribution were characterized by the Breneur–Emmet–Teller (BET) method

based on adsorption data under N_2 at 77.35 K with a Quantachrome NovaWin. Raman spectra were quantified using a Renishaw Company Micro Raman spectrometer with a laser source with a wavelength of 532 nm. The crystallite composition of the samples was analyzed by X-ray diffraction (XRD) using a Rigaku X-pert Pro with Cu Ka radiation λ = 1.5418740 Å. To estimate the crystallite size from the XRD test, we used the Bragg formula (Eq (1)), where n is an integer representing the order of diffraction, λ is the wavelength of the incident X-ray, d is the distance between crystal planes, and θ is the angle of incidence.

$$n\lambda = 2d \sin\theta \tag{1}$$

The classical Debye–Scherer formula was then used to calculate the atom lattice height (L_c) for the structural parameters as follows [38]:

$$L_c = 0.9\lambda/\beta_{002} \cos\theta_{002} \tag{2}$$

$$L_a = 1.94\lambda/\beta_{100/101} \cos\theta_{100/101} \tag{3}$$

$$n = L_c/d_{002} \tag{4}$$

where L_c and L_a are the average apparent crystallite height and diameter dimensions, obtained from the widths of (002) and (100/101) profiles, and d_{002} represents the pseudographitic interlayer spacing.

2.3. Electrochemical measurements

The cathode was prepared by depositing a slurry of 85 wt% prepared CACN as the main active material, 5 wt% Super-P carbon black as conductive additive, and 10 wt% polyvinylidene fluoride (PVDF) as a binder dissolved in dimethyl acetamide (DMAc) solution. To form a homogeneous slurry, the mixture was stirred using a hot plate stirrer at 1000 rpm for 6 h at 60 °C. The slurry was then coated on aluminum foil with a doctor blade, and a preheating treatment was applied overnight at 80 °C. The electrode was pressed using a roller press machine and then cut into a 1 cm^2 circle shape using an electrode cutter; the drying process then continued in a vacuum chamber at 120 °C for 4 h. LTO-based electrodes were also prepared using the same procedure with different compositions, namely 80 wt% LTO (brought from Samsung.co), 10 wt% Super-P, and 10 wt% PVDF, and were then coated with copper foil. 2032-coin cells, labeled LICN200, LICN300, and LICN400, were assembled by placing the anode, separator, and cathode in series with 1 M $LiPF_6$ electrolyte in ethylene carbonate and ethyl methyl carbonate (EC:EMC = 3:7) inside a glove box.

All electrochemical tests were performed at room temperature. Cycling voltammetry (CV) was performed with an electrochemical voltage window of 1–3 V at various scan rates of 5, 10, 15, 25, and 50 mV/s. Galvanostatic charge-discharge (CD) tests were conducted by applying a rate of 2 °C for 100 cycles, with current densities of 4.3, 5.7, and 5.8 mA cm^{-2}, with the theoretical capacitance of activated carbon and the mass of each active material as the calculation reference. The specific capacitance C_s (F/g) of LIC was calculated using the following formula:

$$C_s = \frac{\int I dv}{2 \times m \times v(V_f - V_i)} \tag{5}$$

where $\int I\,dv$ (A) is the total current under the integrated area on the CV graph, m (g) is the total

mass of the cathode active material, v (mV/s) is the applied scan rate, and $(V_f - V_i)$ (V) is the CV test voltage window. The specific power density P (W kg^{-1}) and energy density E (Wh kg^{-1}) of LIC were calculated using the following formulas [11,24]:

$$P = (U \times \frac{i}{m}) \tag{6}$$

$$E = (P \times t) \tag{7}$$

where U (V) is the average of the initial and final voltage discharge curve, m (kg) is the total active mass of both electrodes, and t (h) is the discharge time.

3. Results and discussion

The surface morphology of the samples was investigated using SEM, as shown in Figure 2a–c. The three-dimensional carbon framework of CACN200, 300, and 400 appears as thick sheets, honeycombs, and sponge structures. The surface carbon has a good pore distribution related to its uniformity. Generally, while micropores (<2 nm) provide the high specific surface area (SSA) necessary for charge storage, mesopores function as high-speed channels for rapid ion transport [16]. Meanwhile, macropores act as ion reservoirs that ensure a steady supply of electrolyte, effectively shortening diffusion distance and enhancing rate performance. Based on our observation of SEM images, it can be estimated that the pore size of the specimens is mostly distributed, with diameters ranging from 2 to 50 nm, known as mesoporous.

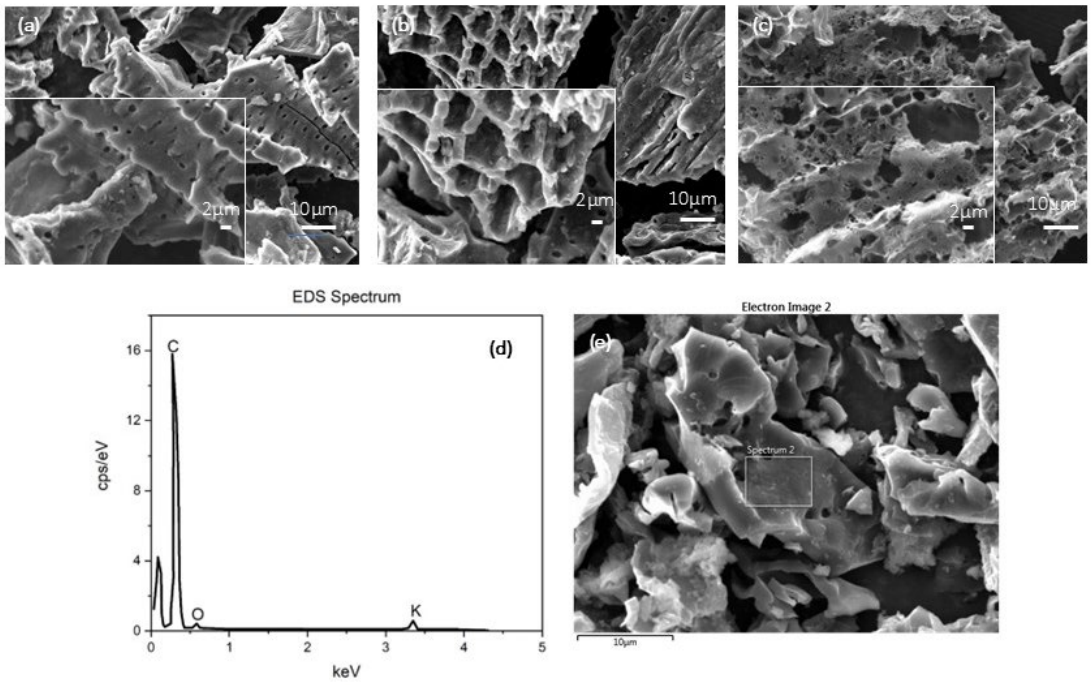

Figure 2. Morphology characterizations by SEM of (a) CACN200, (b) CACN300, (c) CACN400, and (d) EDX test of CACN400 in (e) square spot surface.

Surface elements were also characterized by EDX (only for CACN400) to check the presence of impurities, as can be seen in Figure 2d–e. According to the EDX results, at the selected spot, the carbon (C) component is 94.4%, which represents medium-high purity. On the EDX graph, we can still detect oxygen (O; 3.5%) and potassium (K; 1.1%), which are estimated to originate from salt and silicon (Si 0.6%) impurities, naturally occurring in plants.

The crystallite structure and microstructural parameters of the samples were tested by XRD, as shown in Figure 3. The X-ray diffraction pattern shows no prominent peaks, representing a perfect crystal structure for all samples. The obtained activated carbon showed typical amorphous carbon that maintains poor crystallinity [39]. However, some tiny peaks dominated the XRD graph at 2θ = ~26.3°, ~42.4°, and ~44.4°, corresponding to the (002), (100), and (101) planes of graphite. These are in good agreement with the graphite 2c phase as given by the Crystallography Open Database (COD) card No. 96-101-1061, which has a hexagonal structure of a = 2.74 Å and c = 6.79 Å.

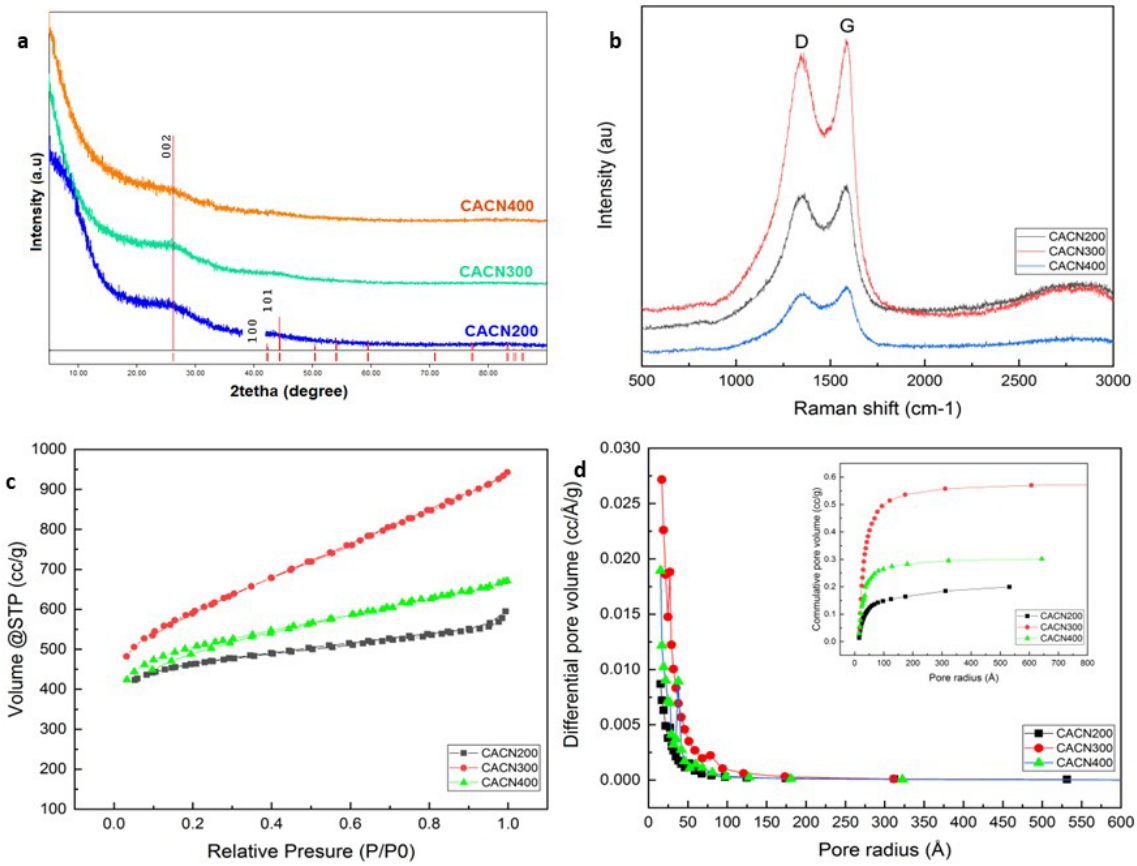

Figure 3. (a) XRD pattern, (b) Raman spectra, (c) N_2 adsorption isotherm, and (d) pore size distribution of CACN based on the BJH method.

The average crystallite size of the samples is approximately 0.33 nm, calculated using the Bragg formula (Eq (1)), supporting the formation of microporosity [38]. The Debye–Scherer formula (Eqs (2)–(4)) was used to calculate the atom lattice height (L_c), as we can observe the alteration of the carbon structure when the N_2 flow rate is varied. Overall, the change in N_2 flow rate directly affects the atom lattice (as shown in detail in Table 1); the smallest L_c occurred for CACN300 (34 nm).

Table 1. XRD calculations using Bragg and Debye–Scherrer formulas, Raman shift, and specific surface area (SSA) from BET results.

Sample	XRD calculation			Raman shift	BET result			
	L_c (nm)	L_a (nm)	d002 (Å)	Id/Ig	SSA_{BET} ($m^2 g^{-1}$)	Pore volume ($cm^3 g^{-1}$)		
						Total	Micro	Meso
CACN200	50.9	114.75	3.395	0.915	1427	0.227	0.042	0.185
CACN300	34	76.48	3.374	0.976	1936	0.661	0.103	0.558
CACN400	40.8	91.83	3.372	0.821	1596	0.374	0.079	0.296

The peaks at ~1570 and ~1350 cm^{-1} from the Raman spectrum of CACN (Figure 3b) represent the G and D bands of the carbon framework, respectively, which are still in the first-order range of all sp2-hybridized carbon. This indicates that the carbon of the sample is amorphous, where the reference G-peak and D-peak of graphite are ~1583 cm^{-1} and ~ 1355 cm^{-1}. These values were further confirmed by C. Sisu C et.al. [40]. Increasing the nitrogen flow rate causes a slight peak shift in the Raman plot. CACN400 has the closest Raman shift for the typical G-band of graphite, followed by CACN300 and CACN200. On the other hand, the D-peak originates from the hybridization vibration mode associated with the edge of graphene, which indicates some interference in the internal structure of graphene [41]. The Id/Ig ratio shows the degree of the carbon atom disorder [42]. The intensity of the defect bands in CACN300 looks more striking than that of the other samples, which implies that its carbon structure is quite random. Referring to our calculations in Table 1, CACN300 has a ratio close to 1; its diffraction homogeneity is the highest, indicating that this sample has the most orderly arrangement of carbon atoms in its crystallite.

All corncob-derived activated carbon appears to have mesoporous and microporous structures, as shown in all graphs exhibiting a typical I adsorption-desorption isotherm (Figure 3c). Increasing the N_2 flow rate during the carbon activation process of carbon did not proportionally increase physical properties, followed by the surface area and pore distribution, as shown in the nitrogen adsorption/desorption graph at 77 K (Figure 3d). The KOH activation mechanism of carbon follows several pathways; the primary general reaction at T > 700 °C is $6KOH + 2C \rightarrow 2K + 3H_2 + 2K_2CO_3$ [34]. This process is the critical step for porosity—the intercalation of potassium (K) into the carbon lattice, which expands the layers, followed by the etching of the carbon framework by the evolved gases and carbonates. At a flow rate of 200 sccm, the kinetic energy of the carrier gas is insufficient to complete activation, and K_2CO_3 and K_2O can form on the surface of the carbon particles, blocking KOH from reaching the interior. Stagnant byproducts, such as H_2O vapor, also likely inhibit deep activation, causing the lowest total pore volume (0.227 cm^3/g). Once the N_2 flow rate was increased from 200 to 300 sccm, excess H_2O and CO_2 were removed, and more metallic K was driven into the carbonized precursor and intercalated into the carbon, wedging apart graphitic layers. Therefore, the surface area and pore volume increased drastically from 1427 $m^2 g^{-1}$ and 0.227 cc g^{-1} to 1936 $m^2 g^{-1}$ and 0.661 cc g^{-1} at 300 sccm. In fact, data shows that the average pore radius of CACN200 of 1.28 nm and CACN300 of 1.51 nm is classified as micropores, while mesopores occupy approximately 81%, increasing to 84%. This occurs because the bound K metal is intercalated at almost the same spot. Conversely, when the N_2 flow rate is modified to 400 sccm as the highest value in this study, the surface area, average pore radius, and pore volume decrease to 1596 $m^2 g^{-1}$, 1.3 nm, and 0.374 $cm^3 g^{-1}$. This is explained by an over-etching event. The aggressive gas flow caused the delicate pore walls to collapse and disordered carbon sites to ablate, thereby decreasing pores and area, reinforced by the resulting pore volume data being smaller than the activation at 300 sccm.

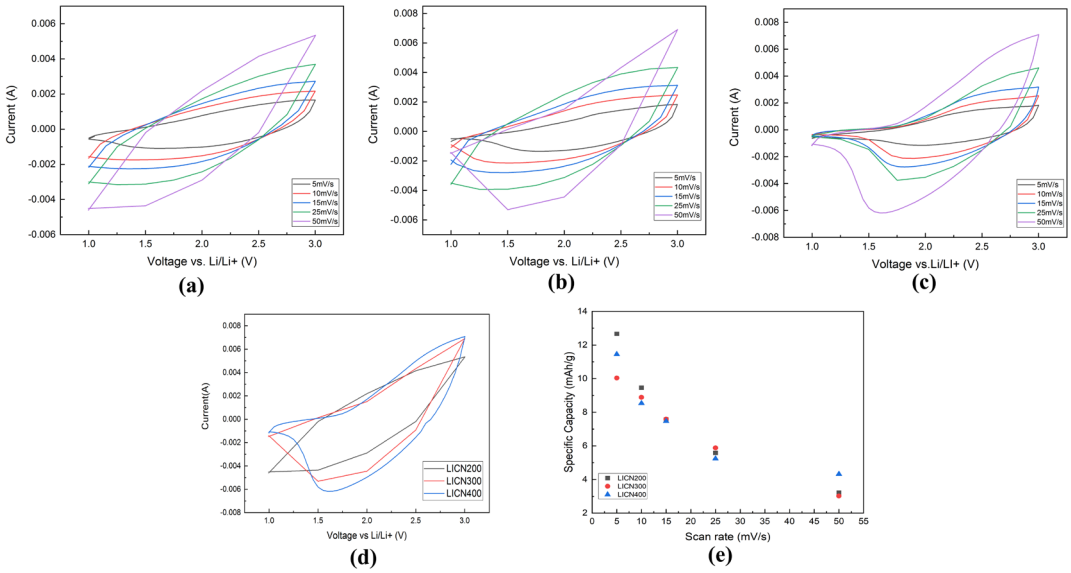

Figure 4. CV graph of (a) LICN200, (b) LICN300, and (c) LICN400; (d) CV graph comparison at 50 mV/s; and (e) the specific capacity of LICNs.

All characterization results indicate that CACN200, 300, and 400 present key advantages as LIC cathode active materials, with small crystallite size, good size uniformity in micropore scale, high pore volume, and high SSA. To evaluate the capability of CACNs, a full LIC cell was constructed with LTO as the anode active material of a 2032 coin cell, denoted as LICN. Cyclic voltammetry (CV) graphs show LICN200, LICN300, and LICN400 (Figure 4a–c) in a voltage window of 1–3 V, where the current increases with increasing voltage sweep rate, at either forward or reverse scan. However, a slight difference was observed in the case of LICN300 using a scan rate of 50 mV/s, where the peak current during reverse scan is higher than that at a 25 mV/s scan rate. This is a potential distortion that may occur at high scan rates due to electrode polarization and faradaic limits during galvanostatic cycling using high power as a parameter [24]. Additionally, this demonstrates capability as a direct consequence of its predominance of mesopores in CACN300 (84.42%), higher than for CANC200 and CACN400, which mitigates the ion diffusion typically observed in purely microporous carbon [43]. The mesopores serve as a low-resistance ion highway and ensure that the Faradaic and capacitive charge-storage sites remain accessible even under high-power demands, allowing for rapid charge/discharge kinetics and higher current densities [43–45]. The different characteristics of CACN as a cathode material make the CV results also very distinctive, as shown in Figure 4d; at a scan rate of 50 mV/s, LICN400 has the most curved form, due to the redox process, and the highest peak current. Figure 4e shows the comparison of the specific capacitance of LICN obtained using Eq (5). The highest specific capacity of all LICN cells is achieved at the lowest scan rate because the formed diffusion layer is wider and the working ions have enough time to penetrate deeper into the electrode material lattice [46]. The remaining challenge of LIC as an energy storage relates to the transfer of working ions using high-speed scan rates. LICN400 has the highest specific capacity at the highest scan rate, which means LICN400 has the best ion transfer rate capability compared to others (data presented in Table 2). We suspect this is due to the CACN400 having a higher percentage of micropores in volume than the other samples (21.12%) and a high graphitic order, since it has the lowest Id/Ig, as shown in

the BET and Raman test results in Table 1. While a high micropore volume typically risks slow kinetics, the low Id/Ig ratio provides better conductivity to facilitate rapid charge transport [47]. This result mitigates the polarization and diffusion limitations observed in the other sample at 50 mV/s and enables better specific capacity retention under high-power conditions.

Table 2. Results of the specific capacity and energy density of LICN.

LIC	Specific capacity at 50 mVs^{-1} ($mAh\,g^{-1}$)	Power density ($W\,kg^{-1}$)	Energy density ($Wh\,kg^{-1}$)	Coulombic efficiency at 100^{th} cycle (%)
LICN200	3.214	376.92	10.2	98.3
LICN300	3.021	526.39	10.79	96.9
LICN400	4.325	427.48	8.11	94.1

The curves shown in Figure 4a–d do not exhibit typical capacitor or battery behaviors but display a quasi-rectangular profile characteristic of LICs, which integrate the hybridization mechanism of capacitors and batteries. During the charging process, electrons from an external power source at a certain voltage accumulate at the anode. Oxidation occurs where Li^+ ions are intercalated into the LTO lattice (faradaic reaction), while $PF6^-$ ions are adsorbed to the cathode-electrolyte interface (non-faradaic reaction) [28]. The accumulation of ions and anions on both sides of the electrode generates polarization, and different potentials are formed. During the discharging process, the load is attached to the LIC, and the different potentials between the electrodes will cause electron/current flow to the load. The reduction process occurs at the anode, with de-intercalation of Li^+ ions back into the electrolyte, while the desorption of $PF6^-$ anions occurs from the cathode-electrolyte interface. Cyclic voltammograms, as given in Figure 4, provide further information regarding these processes, which can be observed from the anode and/or cathode peaks at 1.5 V. These peaks indicate Li-insertion and de-intercalation occurring at the electrode surface and correspond to the formation of an electrical double layer at the electrolyte-electrode interface [48].

The cyclic performance of LICNs over 100 cycles is presented in Figure 5. The LICN200 cell appears to have the highest capacitance, reaching 20.129 $mAh\,g^{-1}$. This high initial capacity is due to the high surface accessibility and pseudocapacitive contribution associated with a moderate value of Id/Ig, which promotes rapid ion adsorption despite the lowest surface area and power volume [49]. Although the coulombic efficiency (CE) at the 100th cycle reaches 98%, while degradation reaches 20.67%, the cell is experiencing unstable performance after the 65th cycle (Figure 5a), and its capacitance also declines [50]. This poor stability stems from a limited pore volume (lower than the other samples), which fails to buffer mechanical stress during cycling, leading to structural fatigue, depletion, or pore clogging that causes rapid capacity decay [51].

The performance trend of LICN400 cells is not significantly distinct from the other cells in terms of specific capacitance alteration, with a slight increase at the end of the cycle, reaching 11.6 $mAh\,g^{-1}$. CACN400 exhibits the lowest Id/Ig ratio, indicating a more ordered (pseudo-graphitic) structure than the other samples. Gradual wetting occurs as layers that may be tightly packed or slightly hydrophobic (water-repelling) require more time for the electrolyte to penetrate. As cycling progresses, the electrical field facilitates ion transport into deeper micropores, gradually increasing the active surface area [52,53]. Nonetheless, the cyclic stability performance of the cell is unstable after the 50th cycle, as seen in Figure 5c. Incomplete ion extraction during previous cycles contributes to additional ion extraction in subsequent cycles (>100%). Additionally, the accumulation of electrolyte

decomposition products and SEI creates high internal resistance and clogs these pathways, leading to the observed instability.

LICN300 has an initial specific capacitance of 11.382 mA hg^{-1}. As shown in Figure 5b, capacitance increases in the first five cycles before gradually decreasing, which is common for energy storage systems. Among all samples, LICN300 demonstrates the best performance, with a specific capacity degradation of only 9.24%. Regarding CE, LICN300 maintains stable performance and provides capacitance for ion movement and storage. The CACN300 has the highest SSA, providing the highest area for charge storage; it also presents high Id/Ig, indicating a defect-rich structure that facilitates rapid ion entry. Furthermore, the dominant mesoporous structure in CACN300 serves as a faster ion reservoir, ensures immediate electrolyte wetting, and provides a good mechanical buffer. This optimized pore network enables ions to access active sites effectively, even at high power density, resulting in a stable CE of 97%. The Ragone plot of LICNs over five sampling cycles is presented in Figure 5d. The combination of good crystallinity, high SSA, and high porosity enables LICN300 to optimize ion movement and displacement within the structure, delivering superior power and energy density [54]. LICN300 achieves the highest average energy density of 10.79 Wh kg^{-1} at 526.39 W kg^{-1}. In comparison, LICN200 and LICN400 deliver energy densities of 10.2 Wh kg^{-1} at 376.92 W kg^{-1} and 8.11 Wh kg^{-1} at 427.48 W kg^{-1}, respectively, as shown in Table 2.

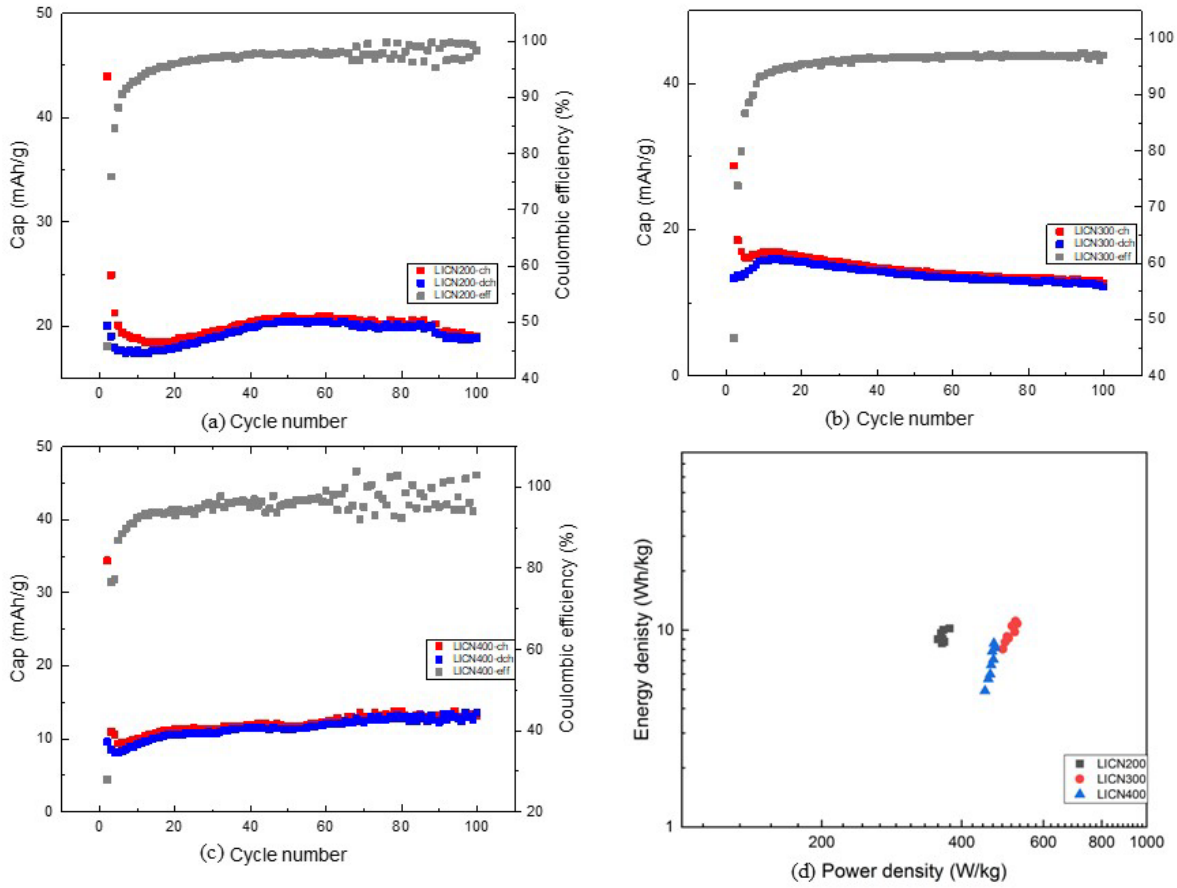

Figure 5. Cycling performance from the CD test of (a) LICN200, (b) LICN300, and (c) LICN400, and (d) comparison of LICN energy and power density on the Ragone plot.

4. Conclusions

Corncob-derived activated carbon was successfully synthesized and applied as an active LIC material. Variating the nitrogen gas flow rate had a positive effect on the physical properties of CACN, where 300 sccm led to the best physical properties, with high pore structure, the highest SSA (1936 $m^2 g^{-1}$), and the smallest crystallite size. LICN300 constructed with CACN300 provided the best electrochemical performance with great Coulomb stability, while energy density was 10.79 Wh kg^{-1} at 526.39 W kg^{-1}. CACN at a higher flow rate could provide better LIC capacity, but it was unstable in a high charge-discharge cycle. Therefore, this study offers a new approach to optimizing the physical properties of AC from agricultural waste. Using this simple method presents advantages for high electrochemical performance by the active material of lithium-ion capacitors (LICs).

Use of AI tools declaration

During the preparation of this work, the authors used Google Gemini in order to improve the sentence structure and readability. Following the use of this tool, the authors reviewed and edited the content as needed and take full responsibility for the content of the publication.

Acknowledgments

This work has been supported by USAID through Sustainable Higher Education Research Alliances (SHERA) Project for Universitas Indonesia's SMART CITY Center for Collaborative Research (No. 0144/UN2.R3.SC/HKP.05.01/2018).

Conflict of interest

The authors declare no conflicts of interest.

Author contributions

Conceptualization, Asih Kurniasari; Methodology, Asih Kurniasari; Sample preparation, Testing, and Data curation, Asih Kurniasari, Ariono Verdianto; Formal analysis, Asih Kurniasari; Writing—original draft preparation, Asih Kurniasari; Writing—reviewing and editing, Chairul Hudaya, Asih Kurniasari; Visualization, Asih Kurniasari; Supervision, Chairul Hudaya, Yoyok Dwi Setyo Pambudi; Funding acquisition, Chairul Hudaya.

References

1. Niu H, Zhang N, Lu Y, et al. (2024) Strategies toward the development of high-energy-density lithium batteries. *J Energy Storage* 88: 111666. https://doi.org/10.1016/J.EST.2024.111666
2. Li M, Lu J, Chen Z, et al. (2018) 30 years of lithium-ion batteries. *Adv Mater* 30: 1800561. https://doi.org/10.1002/adma.201800561

3. Pambudi YDS, Setiabudy R, Yuwono AH, et al. (2019) Effects of annealing temperature on the electrochemical characteristics of ZnO microrods as anode materials of lithium-ion battery using chemical bath deposition. *Ionics* 25: 457–466. https://doi.org/10.1007/s11581-018-2723-z
4. Venkatesh M, Amit Kumar Thakur, Lovi Raj Gupta, et al. (2024) A comprehensive review of concepts, benefits, and challenges of a battery-powered aircraft. *Evergreen* 11: 1901–1918. https://doi.org/10.5109/7236841
5. Hasan MM, Haque R, Jahirul MI, et al. (2025) Advancing energy storage: The future trajectory of lithium-ion battery technologies. *J Energy Storage* 120: 116511. https://doi.org/10.1016/J.EST.2025.116511
6. Diantoro M, Nasikhudin, Suryana R, et al. (2024) Addition of Al_2O_3 to the Al_2O_3/AC//Si electrode to enhance the performance of supercapattery. *Evergreen* 11: 2081–2090. https://doi.org/10.5109/7236853
7. Aziz SB, Brza MA, Abdulwahid RT, et al. (2023) Electrochemical properties of a novel EDLC derived from plasticized biopolymer based electrolytes with valuable energy density close to NiMH batteries. *Sci Rep* 13: 21139. https://doi.org/10.1038/s41598-023-48417-6
8. Burke AF, Zhao J (2022) Development, performance, and vehicle applications of high energy density electrochemical capacitors. *Appl Sci* 12: 1726. https://doi.org/10.3390/app12031726
9. Jeżowski P, Crosnier O, Deunf E, et al. (2018) Safe and recyclable lithium-ion capacitors using sacrificial organic lithium salt. *Nat Mater* 17: 167–173. https://doi.org/10.1038/nmat5029
10. Wang Y, Xue K, Zhang X, et al. (2023) High-voltage electrochemical double layer capacitors enabled by polymeric ionic liquid. *Electrochim Acta* 441: 141829. https://doi.org/10.1016/J.ELECTACTA.2023.141829
11. Sun F, Gao J, Zhu Y, et al. (2017) A high performance lithium-ion capacitor achieved by the integration of a Sn-C anode and a biomass-derived microporous activated carbon cathode. *Sci Rep* 7: 40990. https://doi.org/10.1038/srep40990
12. Agrawal R, Chen C, Dages S, et al. (2016) Lithium-ion capacitor based on electrodes constructed via electrostatic spray deposition. *ECS Trans* 72: 45–53. https://doi.org/10.1149/07208.0045ecst
13. Lamb JJ, Burheim OS (2021) Lithium-ion capacitors: A review of design and active materials. *Energies* 14: 979. https://doi.org/10.3390/en14040979
14. Song T, Zhao Y, Chen C, et al. (2024) Recyclable NaCl template assisted preparation of N/O co-doped porous carbon for zinc-ion hybrid capacitor. *J Energy Storage* 98: 113148. https://doi.org/10.1016/j.est.2024.113148
15. Xu H, Ni J, Chen W, et al. (2025) Nitrogen and oxygen co-doped porous carbon tubes with fast ion diffusion channel for supercapacitor. *Energy Technol* 14: e202501597. https://doi.org/10.1002/ente.202501597
16. Qiao L, Chen W, Zhao Y, et al. (2026) Recrystallization template method to construct B/N co-doped hierarchically porous carbon for supercapacitor and zinc ion hybrid capacitor. *J Energy Storage* 141: 119336. https://doi.org/10.1016/j.est.2025.119336
17. Xu H, Ni J, Liu M, et al. (2026) Boron-enriched edge-nitrogen doped porous carbon nanosheets as cathode for zinc-ion hybrid capacitors. *J Taiwan Inst Chem Eng* 181: 106511. https://doi.org/10.1016/j.jtice.2025.106511
18. Amatucci GG, Badway F, Du Pasquier A, et al. (2001) An asymmetric hybrid nonaqueous energy storage cell. *J Electrochem Soc* 148: A930. https://doi.org/10.1149/1.1383553

19. Ruan D, Kim MS, Yang B, et al. (2017) 700 F hybrid capacitors cells composed of activated carbon and $Li_4Ti_5O_{12}$ microspheres with ultra-long cycle life. *J Power Sources* 366: 200–206. https://doi.org/10.1016/J.JPOWSOUR.2017.09.029
20. Zhao B, Ran R, Liu M, et al. (2015) A comprehensive review of $Li_4Ti_5O_{12}$-based electrodes for lithium-ion batteries: The latest advancements and future perspectives. *Mater Sci Eng R Rep* 98: 1–71. https://doi.org/10.1016/J.MSER.2015.10.001
21. Zhao S, Sun X, Wang N, et al. (2024) Recent advances in hybrid lithium-ion capacitors: Materials and processes. *ACS Appl Energy Mater* 7: 11553–11570. https://doi.org/10.1021/acsaem.4c00230
22. Chen C, Agrawal R, Wang C (2015) High performance $Li_4Ti_5O_{12}$/Si composite anodes for Li-ion batteries. *Nanomaterials* 5: 1469–1480. https://doi.org/10.3390/nano5031469
23. Gangaja B, Nair S, Santhanagopalan D (2024) $Li_4Ti_5O_{12}$-TiO_2 composite anode for high performance full-cell Li-ion battery and Li-ion capacitor applications. *Discov Electrochem* 1: 5. https://doi.org/10.1007/s44373-024-00002-w
24. Li B, Zhang H, Wang D, et al. (2017) Agricultural waste-derived activated carbon for high performance lithium-ion capacitors. *RSC Adv* 7: 37923–37928. https://doi.org/10.1039/C7RA06680E
25. Eleri OE, Lou F, Yu Z (2023) Lithium-ion capacitors: A review of strategies toward enhancing the performance of the activated carbon cathode. *Batteries* 9: 533. https://doi.org/10.3390/batteries9110533
26. Gao X, Zhan C, Yu X, et al. (2017) A high performance lithium-ion capacitor with both electrodes prepared from Sri Lanka Graphite Ore. *Materials* 10: 414. https://doi.org/10.3390/ma10040414
27. Liu C, Koyyalamudi BB, Li L, et al. (2016) Improved capacitive energy storage via surface functionalization of activated carbon as cathodes for lithium-ion capacitors. *Carbon* 109: 163–172. https://doi.org/10.1016/j.carbon.2016.07.071
28. Sennu P, Arun N, Madhavi S, et al. (2019) All carbon based high energy lithium-ion capacitors from biomass: The role of crystallinity. *J Power Sources* 414: 96–102. https://doi.org/10.1016/j.jpowsour.2018.12.089
29. Zhang Y, Sheng L, Zhao C, et al. (2025) Tailored biomass-derived porous carbon with dual-activator for high-mass-loading supercapacitors with enhanced rate capabilities. *J Energy Storage* 136: 118601. https://doi.org/10.1016/j.est.2025.118601
30. Malini K, Selvakumar D, Kumar NS (2023) Activated carbon from biomass: Preparation, factors improving basicity and surface properties for enhanced CO_2 capture capacity—A review. *J CO_2 Util* 67: 102318. https://doi.org/10.1016/j.jcou.2022.102318
31. Azargohar R, Dalai AK (2006) Biochar as a precursor of activated carbon. *Appl Biochem Biotechnol* 131: 762–773. https://doi.org/10.1385/ABAB:131:1:762
32. Magar SD, Leibing C, Gómez-Urbano JL, et al. (2023) Brewery waste derived activated carbon for high performance electrochemical capacitors and lithium-ion capacitors. *Electrochim Acta* 446: 142104. https://doi.org/10.1016/j.electacta.2023.142104
33. Purnomo CW, Widyadhana A (2020) Lithium and calcium recovery by activated carbon from coconut shell char. *IOP Conf Ser Mater Sci Eng* 823: 012032. https://doi.org/10.1088/1757-899X/823/1/012032
34. Wang J, Kaskel S (2012) KOH activation of carbon-based materials for energy storage. *J Mater Chem* 22: 23710. https://doi.org/10.1039/c2jm34066f

35. Hui TS, Zaini MAA (2015) Potassium hydroxide activation of activated carbon: A commentary. *Carbon Lett* 16: 275–280. https://doi.org/10.5714/CL.2015.16.4.275
36. Li H, Ma Y, Wang Y, et al. (2024) Nitrogen enriched high specific surface area biomass porous carbon: A promising electrode material for supercapacitors. *Renewable Energy* 224: 120144. https://doi.org/10.1016/j.renene.2024.120144
37. KaruniaBr E (2024) Inovasi pemanfaatan limbah tongkol jagung menjadi biochar sebagai adsorben slow release fertilizer. Available from: https://www.kompasiana.com/ermakaruniabrginting/666f232fed64153c0748ebe3/inovasi-pemanfaatan-limbah-tongkol-jagung-menjadi-biochar-sebagai-adsorben-slow-release-fertilizer.
38. Girgis BS, Temerk YM, Gadelrab MM, et al. (2007) X-ray diffraction patterns of activated carbons prepared under various conditions. *Carbon Lett* 8: 95–100. https://doi.org/10.5714/CL.2007.8.2.095
39. Aboud M, ALOthman Z, Habila M, et al. (2015) Hydrogen storage in pristine and d10-block metal-anchored activated carbon made from local wastes. *Energies* 8: 3578–3590. https://doi.org/10.3390/en8053578
40. Sisu C, Iordanescu R, Stanciu V, et al. (2016) Raman spectroscopy studies of some carbon molecular sieves. *Dig J Nanomater Bios* 11: 435–442. Available from: https://www.imrpress.com/journal/DJNB/article/11/2/pii/S1842-3582(26)01457-0.
41. Wu JB, Lin ML, Cong X, et al. (2018) Raman spectroscopy of graphene-based materials and its applications in related devices. *Chem Soc Rev* 47: 1822–1873. https://doi.org/10.1039/C6CS00915H
42. Dresselhaus MS, Jorio A, Souza Filho AG, et al. (2010) Defect characterization in graphene and carbon nanotubes using Raman spectroscopy. *Philos Trans A Math Phys Eng Sci* 368: 5355–5377. https://doi.org/10.1098/rsta.2010.0213
43. Bulakhe RN, Nguyen AP, Ryu C, et al. (2023) Facile synthesis of mesoporous nanohybrid two-dimensional layered Ni-Cr-S and reduced graphene oxide for high-performance hybrid supercapacitors. *Materials* 16: 6598. https://doi.org/10.3390/ma16196598
44. Pan Z, Yu S, Wang L, et al. (2023) Recent advances in porous carbon materials as electrodes for supercapacitors. *Nanomaterials* 13: 1744. https://doi.org/10.3390/nano13111744
45. Bang JH, Lee BH, Choi YC, et al. (2022) A study on superior mesoporous activated carbons for ultra power density supercapacitor from biomass precursors. *Int J Mol Sci* 23: 8537. https://doi.org/10.3390/ijms23158537
46. Elgrishi N, Rountree KJ, McCarthy BD, et al. (2018) A practical beginner's guide to cyclic voltammetry. *J Chem Educ* 95: 197–206. https://doi.org/10.1021/acs.jchemed.7b00361
47. Lu X, Lian GJ, Parker J, et al. (2024) Effect of carbon blacks on electrical conduction and conductive binder domain of next-generation lithium-ion batteries. *J Power Sources* 592: 233916. https://doi.org/10.1016/j.jpowsour.2023.233916
48. Puthusseri D, Aravindan V, Madhavi S, et al. (2014) Improving the energy density of Li-ion capacitors using polymer-derived porous carbons as cathode. *Electrochim Acta* 130: 766–770. https://doi.org/10.1016/j.electacta.2014.03.079
49. Balaji Mohan V, Liu D, Jayaraman K, et al. (2016) Improvements in electronic structure and properties of graphene derivatives. *Adv Mater Lett* 7: 421–429. https://doi.org/10.5185/amlett.2016.6123

50. Ferrari AC, Robertson J (2000) Interpretation of Raman spectra of disordered and amorphous carbon. *Phys Rev B* 61: 14095–14107. https://doi.org/10.1103/PhysRevB.61.14095
51. Xiao L, Lu H, Fang Y, et al. (2018) Low-defect and low-porosity hard carbon with high coulombic efficiency and high capacity for practical sodium ion battery anode. *Adv Energy Mater* 8: 1703238. https://doi.org/10.1002/aenm.201703238
52. Zhu Y, Murali S, Stoller MD, et al. (2011) Carbon-based supercapacitors produced by activation of graphene. *Science* 332: 1537–1541. https://doi.org/10.1126/science.1200770
53. Suhas, Chaudhary M, Chaudhary S, et al. (2025) Transforming biomass waste into hydrochars and porous activated carbon: A characterization study. *Resources* 14: 34. https://doi.org/10.3390/resources14030034
54. Zhang T, Zhang F, Zhang L, et al. (2015) High energy density Li-ion capacitor assembled with all graphene-based electrodes. *Carbon* 92: 106–118. https://doi.org/10.1016/j.carbon.2015.03.032

AIMS Press